

Accepted Article

Microseismicity indicates atypical small-scale plate rotation at the Quebrada transform fault system, East Pacific Rise

Jianhua Gong¹, Wenyuan Fan¹, & Ross Parnell-Turner¹

¹Scripps Institution of Oceanography, UC San Diego, La Jolla, California 92093, USA

Key Points:

- Four segments of Quebrada transform system show significantly different seismic intensities.
- One fracture zone segment appears to be seismogenic indicating local plate rotation.
- Deep clouds of seismicity extend into the uppermost mantle at spreading center-transform fault intersections.

Corresponding author: Jianhua Gong, j4gong@ucsd.edu

This article has been accepted for publication and undergone full peer review but has not been through the copyediting, typesetting, pagination and proofreading process, which may lead to differences between this version and the Version of Record. Please cite this article as doi: 10.1029/2021GL097000.

This article is protected by copyright. All rights reserved.

Abstract

Closely-spaced, multi-strand ridge transform faults (RTFs) accommodate relative motions along fast spreading mid-ocean ridges. However, the relations between RTFs and plate spreading dynamics are poorly understood. The Quebrada system is one of the most unique RTF systems at the East Pacific Rise, consisting of four transform faults connected by three short intra-transform spreading centers (ITSCs). We use seven-months of ocean bottom seismograph data to study the Quebrada system, and find abundant earthquakes unevenly distributed among three active faults. We identify two deep, diffuse seismicity clouds at the inside corners of the ITSC-transform fault intersections, and one seismically active fracture zone. The observations suggest a complex regional plate-motion pattern, including possible heterogeneous rotations within the Quebrada system. Evolution of multi-strand RTFs may have resulted from a strong three-dimensional local thermal and fluid effects, while the RTFs may have also regulated regional tectonics, forming an intricate feedback system.

Plain Language Summary

Mid-ocean ridge transform faults (RTFs) are plate boundaries that offset adjacent mid-ocean ridges. At fast spreading mid-ocean ridges, such as the East Pacific Rise, closely spaced, multi-strand RTFs are often connected by two or more short intra-transform spreading centers (ITSCs). However, physical processes accommodating plate spreading along such multi-strand RTF systems and the inter-relations between the fault system and the tectonic dynamics are not well understood. Quebrada is one of such multi-strand RTFs at the East Pacific Rise. We utilize seven-month seismic data from ocean bottom seismographs of a 2008 experiment to investigate the seismotectonics of the region. We find intriguing, abundant seismicity on one of the fracture zones, contradicting the traditional view that fracture zones are seismically quiescent. Further, we identify two diffuse seismicity clouds penetrating the uppermost mantle at the inside corners of the ITSC-transform fault intersections, implying complex interactions among ITSCs, transform faults, and their surrounding structure. From these observations, we infer that there are rotational motions within the Quebrada fault system, which have caused slip along the fracture zone and facilitated fluid circulations to produce deep, diffuse seismicity. We speculate that there is a complex feedback system between the multi-strand RTFs and local three-dimensional tectonic processes.

1 Introduction

Mid-ocean ridge transform faults (RTFs) play a key role in plate tectonics, by offsetting spreading segments and thus accommodating relative motion between adjacent oceanic plates. These RTFs also form fracture zones, which are fossil fault traces located outside the inter-spreading regions, which are rarely reactivated except occasionally in close proximity to subduction zones (Hall et al., 2003; Robinson, 2011; Lange et al., 2010; Contreras-Reyes & Carrizo, 2011). The lengths of RTFs vary from ~30 km to ~1000 km (Bird, 2003), and most of the motion along RTFs is aseismic slip (Boettcher & Jordan, 2004; Boettcher & McGuire, 2009; Shi et al., 2021). Characteristic earthquakes (~M6) at RTFs show some of the most systematic and predictable rupture behaviors on Earth (McGuire, 2008; McGuire et al., 2012; Kuna et al., 2019). For example, M6 strike-slip earthquakes occur quasi-periodically every 5–6 years on the Gofar RTF in the equatorial East Pacific Rise, and it is thought that these earthquakes repeatedly break the same fault patches (McGuire et al., 2012). RTFs such as Gofar are well-documented, however most multi-strand RTFs, i.e. those consisting of several transforms separated by small intra-transform spreading centers (ITSCs), are less well understood. Although multi-strand RTFs are fairly common along spreading centers such as the East Pacific Rise (EPR), little is known about the relations between multi-strand RTFs and the thermal structure

and tectonic processes at mid-ocean ridges (P. J. Fox & Gallo, 1984; Parmentier & Forsyth, 1985; Morgan & Forsyth, 1988; Gregg et al., 2009; Wolfson-Schwehr et al., 2017).

The Quebrada-Discovery-Gofar transform fault system on the East Pacific Rise at $\sim 4^\circ\text{S}$ includes eight ITSCs, which accommodate plate spreading at a half-rate of $\sim 70 \text{ mm/yr}$ (Searle, 1983). The Gofar and Discovery systems have three and two fault segments bounding two and one ITSCs, respectively. The Quebrada fault system has four fault segments and three ITSCs. The Gofar and Discovery systems are comparable in size and kinematic setting, and both have physical features typical of a RTF system, including varying degrees of seismic coupling along strike, and frequent characteristic earthquakes (McGuire et al., 2012; Wolfson-Schwehr et al., 2014; Guo et al., 2018; Kuna et al., 2019). A one-year ocean bottom seismograph (OBS) deployment on the Gofar and Discovery faults identified seismic zones hosting regular M6 earthquakes, and aseismic zones primarily hosting microseismicity (McGuire et al., 2012; Guo et al., 2018). These observations suggest that slip can occur either fast or slowly on these faults, and that no portion of the segments is fully locked (Boettcher & Jordan, 2004; McGuire et al., 2012; Wolfson-Schwehr & Boettcher, 2019).

Despite being located only $\sim 37 \text{ km}$ from the northern end of the Discovery fault segment, the seismicity and morphology of the Quebrada fault system differ from those of the Gofar and Discovery systems (Pickle et al., 2009). Between 1990 and 2008, only one $M > 5.5$ earthquake occurred in the Quebrada fault system ($M 5.6$, 2003/12/19), while the Gofar and Discovery faults hosted 30 $M \geq 5.5$ earthquakes (C. G. Fox et al., 2001; McGuire, 2008). This contrasting seismogenic behavior suggests that different processes may be at play at Quebrada, and that its faulting configuration may be more complex than the idealized strike-slip motion as for other RTF systems. Here we use seismic records from 11 OBSs to study the Quebrada transform system, which were part of a larger network, deployed to monitor seismicity across the whole Quebrada-Discovery-Gofar system from December 2007 to February 2009 (McGuire et al., 2012; Wolfson-Schwehr et al., 2014). We detect and locate earthquakes of the fault system and investigate the relations between the seismicity and regional tectonic processes. Our collective observations suggest that the seismicity may represent small-scale plate rotations and that multi-strand transform systems connected by short ITSCs may have played a role in modifying local thermal structure, fluid circulation, and melt migration in the vicinity of the transform system.

2 Quebrada Transform Fault System

The Quebrada transform fault system consists of four fault segments numbered Q1 to Q4 (north to south), extending 42 km, 24 km, 25 km and 30 km, respectively (Figure 1). Fault strands have slightly varying orientation, with an average strike direction of $\sim 102^\circ$. The fault segments slip at a rate of $\sim 123\text{--}140 \text{ mm/yr}$ (Searle, 1983; Wolfson-Schwehr & Boettcher, 2019), and the average fault zone width is about 2 km (Wolfson-Schwehr & Boettcher, 2019). These faults are separated by three ITSCs from north to south (numbered S9, S8 and S7, following convention of Pickle et al., 2009) with lengths of 4 km, 10 km and 7 km, respectively. The across-axis extent of the volcanic terrain associated with individual ITSCs is difficult to define. The axial depths of each ITSC are 3.8–4.2 km, which is deeper than typical fast-spreading mid-ocean ridge segments, such as the one northeast of Q1, which is $\sim 3 \text{ km}$ deep. There are several basins associated with S9, Q2 and S8 – water depths are up to 4600 m, and the water depth near S7 is $\sim 4000 \text{ m}$. The Quebrada transform system is bounded by high relief flanks (north and south flanks in Figure 1) on both the north and south sides with a water depth range of 2500–3000 m (Pickle et al., 2009). In contrast, the depths near S6 and EPR are about 3200 m.

The Quebrada transform fault system has several unique geological and geophysical features, distinguishing itself from other typical RTFs. For example, residual mantle Bouguer anomalies of the region show that the deep basins around Q2 and S8 have crust only 3–4 km thick (Pickle et al., 2009). Further, the MgO content of rocks dredged from the three ITSCs indicate limited magmatic differentiation during crust generation, possibly due to relatively cool mantle temperatures and low magma supply (Pickle et al., 2009). The most perplexing attribute of the Quebrada fault system is the apparent lack of moderate magnitude ($M > 5.5$) events (McGuire, 2008). Only 73 $M \geq 3$ events that likely occurred in the system (in the region of 104°W – 102.5°W and 4.1°S – 3.45°S , Figure S1) were reported by International Seismological Centre (ISC) from 1 January 1980 to 1 January 2022 (International Seismological Centre, 2021). Given the fast half spreading rate (70 mm/yr) along the Quebrada transform fault, it is unclear how the plate motion is accommodated by the Quebrada faults without generating large magnitude events.

Plate motion and spreading processes regulate deformation between adjacent RTFs, and directly imprint on the morphology of spreading centers connecting these faults. For example, RTFs separated by tens of kilometers are connected by mid-ocean ridges whose axial morphology closely correlates with the plate spreading rate (Macdonald, 1982; Smith & Sandwell, 1997). In contrast, more closely-spaced, subparallel RTFs are commonly connected by step-overs, pull-apart basins, or narrow inter-transform spreading centers at fast spreading mid-ocean ridges, including the Quebrada transform fault system (Menard & Atwater, 1968; Searle, 1983; Wolfson-Schwehr & Boettcher, 2019). It is thought that the origins of such multi-strand RTFs is linked to changes in plate motion directions (Menard & Atwater, 1968; Pockalny et al., 1997). For instance, counter-clockwise spreading-direction rotation between the Pacific and Cocos plates in the past ~ 5 Myr has caused transtension along the left-lateral Siqueiros transform faults, and transpression along the right-lateral Clipperton transform fault (Pockalny et al., 1997; Pockalny, 1997; Van Avendonk et al., 1998, 2001; Gregg et al., 2009). Transpressional stress at Clipperton has generated median ridges along the fault, while transtensional stress at Siqueiros has caused extension within the system, leading to fissures and magma delivery to the seafloor, and forming a pull-apart basin or ITSC. The rotation pattern is the opposite at the Quebrada-Discovery-Gofar system that all the transform faults are left-lateral, requiring a clockwise rotation between the Pacific and Nazca plates.

3 Materials and Methods

3.1 Data

In 2008, an array of 30 broadband and 10 short-period three-component OBSs was deployed on the Quebrada-Discovery-Gofar transform fault system for a period of over 13 months (McGuire et al., 2012). Twelve of the instruments (four broadband and eight short-period stations) were free-fall deployed at the Quebrada transform system, although one station, Q08, did not record useful data (Figure 1). The network consisted of two 30 km aperture arrays, including seven OBSs on Q1 and five OBSs on Q4. The stations were located in water depths ranging from 3300 to 3870 m, and the OBSs recorded waveform data at a sampling rate of 100 Hz. The short period instruments' power supply was exhausted in July 2008 (Table S1), hence we only investigate the operational period from 1 January 2008 to 7 August 2008 (Julian Day 1 to 207) in this study. During the same time period, the ISC catalog reports two $M > 3$ events that occurred near the Quebrada transform system, both happening on 6 January 2008 (Table S2). Detailed data quality descriptions can be found in Text S1.

3.2 Earthquake Detection and Location

We apply a suite of techniques to detect, locate, and relocate earthquakes occurring on the Quebrada transform faults. We first detect seismic body wave arrivals of both

163 *P* and *S* phases using a machine-learning phase picker, EQTransformer (Mousavi et al.,
 164 2020). EQTransformer is a deep-learning model for simultaneous earthquake detection
 165 and phase picking with uncertainty quantification. The method can detect *P* and *S* phases
 166 on single-station records for earthquakes occurring within a local distance, and the un-
 167 certainty of the phase picks are represented as confidence levels (probability). It is trained
 168 on a large-scale dataset with 1 million earthquake records and 300 thousand noise wave-
 169 forms (Mousavi et al., 2019). The earthquake waveforms of the training dataset are mostly
 170 from events recorded within a few hundred kilometers. In contrast, earthquakes of the
 171 Quebrada faults are recorded by stations within tens of kilometers, which results in shorter
 172 S-P times. Therefore, we upsample the seismic records by a factor of two (200 Hz) to
 173 stretch the data before applying the EQTransformer detector. The procedure is simi-
 174 lar to a strategy adopted by Wang et al. (2020) to detect earthquakes using dense nodal
 175 arrays. This approach extends the separation intervals for EQTransformer by assuming
 176 that records remain sampled at 100 Hz, and we later re-scale the detection time to its
 177 true sampling rate. Emergent P-waves are common in OBS data and could be challeng-
 178 ing to pick by autopickers (e.g., McGuire et al., 2012). We find that EQTransformer can
 179 successfully detect emergent P-wave arrivals such as the example shown in Figure S20.
 180 However, this method can miss large magnitude events, such as the two M>3.5 ISC events
 181 on 6 January 2008. Such events have very emergent P-arrivals and are challenging to iden-
 182 tify even for experienced analysts (e.g., Figure S9). For these events, we manually pick
 183 the arrivals for subsequent location steps. In total, we detect ~390,000 *P* arrivals and
 184 ~420,000 *S* arrivals with an average confidence level of 0.5.

185 We then associate the obtained phase picks using an open-source algorithm, REAL
 186 (M. Zhang et al., 2019). REAL uses a grid-search method, and associates the phase picks
 187 and approximately locates a seismic event by counting the number of *P* and *S* picks and
 188 computing the traveltimes residuals. A successful association must meet a predefined pick
 189 threshold within the predicted traveltimes windows from a given velocity model (M. Zhang
 190 et al., 2019). In this study, we require a candidate earthquake having a minimum of 3
 191 *P* arrivals and 4 total phase arrivals with a residual arrival time tolerance of 0.5 s. These
 192 requirements are relaxed comparing to typical onshore earthquake studies (e.g., Wang
 193 et al., 2020) to maximize detection with the sparse network at Quebrada. To ensure the
 194 location robustness, we apply further quality control procedures in later stages (described
 195 below). We use a 1D *P*-wave velocity profile extracted from a *P*-wave travel time tomo-
 196 graphic model for the Quebrada system (Roland et al., 2012) for the association step (Fig-
 197 ure S2). The velocity model approximates typical 2 Myr old oceanic crust and upper-
 198 mantle structure. We assume a constant Vp/Vs ratio of 1.9 for the crust (above 6.85 km
 199 depth) and 1.8 for the mantle (below 6.85 km depth) to obtain a 1D *S*-wave velocity model
 200 for this study. The grid-searching area covers a 0.2° radius region centering at the sta-
 201 tion that records the earliest phase arrival and extends 20 km in depth. The searching
 202 grids are spaced 0.01° horizontally and 0.5 km vertically. In total, we identify 31,501 can-
 203 didate earthquakes from the association step.

204 After making the phase associations, we use COMPLOC (Lin & Shearer, 2005, 2006)
 205 to invert the earthquake locations. The COMPLOC algorithm uses *P*- and *S*-wave ar-
 206 rivel times to locate or relocate earthquakes. It applies a source-specific station term method
 207 to solve for local earthquake locations, which has the advantage of improving the rela-
 208 tive location accuracy of nearby events by empirically correcting the effects of three-dimensional
 209 velocity structures (Richards-Dinger & Shearer, 2000; Lin & Shearer, 2005). The method
 210 is insensitive to phase-pick outliers as we select the ℓ_1 norm to evaluate the travel time
 211 residuals. Given the network configuration, some earthquakes are erroneously located
 212 to the seafloor. We have visually inspected some cases and conclude that these shallow
 213 earthquakes are likely mislocated. Therefore, we iteratively locate earthquakes with COM-
 214 PLOC, and remove events placed within 1 km depth to the seafloor. We improve the earth-
 215 quake locations by running this iterative procedure for 40 times (Figure S3), leading to
 216 23,604 final, successful locations (Figure S4).

The earthquake locations are further refined using the GrowClust relocation method (Trugman & Shearer, 2017). The technique uses differential travel times obtained from cross correlations of P or S waveforms to determine the relative locations of event pairs at high precision. Similar relocation applications have proven crucial in revealing complex fault architectures and impulsive tectonic processes (Waldhauser & Ellsworth, 2000; H. Zhang & Thurber, 2003; Hauksson & Shearer, 2005; Tan et al., 2016; Parnell-Turner et al., 2017; Ross et al., 2019). The GrowClust algorithm is computationally efficient and can adaptively group events into clusters based on their waveform similarities. We only cross correlate P and S waves of the closest 100 events for each earthquake to obtain differential travel times. Such a selection procedure reduces the computational burden, and we successfully relocated 23,593 earthquakes in total (Figure 2).

To evaluate the robustness of the seismicity pattern, we select events with at least 4 P and 4 S picks and apply the same suite of techniques aforementioned. This exercise results in detecting, locating, and relocating $\sim 9,000$ events (Figure S5). The results show similar earthquake distributions as of the full catalog, confirming the fidelity of our results. We further perform synthetic tests on the location results and assess the details in the Discussion.

3.3 Magnitude Calculation

We calculate local magnitude (M_L) of the earthquakes from 3-component displacement waveforms (Gutenberg & Richter, 1956). We first remove the instrument response and convolve the records with the Wood-Anderson instrument response. The waveforms are then filtered between 4–20 Hz and cut from 2 s before to 3 s after the S arrivals of an earthquake. The peak amplitude (A) is calculated as root sum square of the 3-component displacements. We also measure the peak noise amplitude (N) in the same way but using a window of 5 s to 2 s before the P arrivals. We only keep a peak amplitude measurement if its signal to noise ratio (A/N) is greater than 10. The local magnitude is calculated as

$$M_L = \log_{10}(A) + 2.56 \log_{10}(D) - 1.67, \quad (1)$$

where D is the hypocenter distance. A M_L is computed for each S phase measurement for a given event, and the final M_L of the earthquake is estimated as the median value of the population. To assure the robustness, an event is assigned a M_L only when there are more than three qualified S phase measurements. In total, we obtain M_L for 10,120 earthquakes. The magnitude-frequency distribution of the final catalog is shown in Figure S6, which follows a b-value close to 0.93 with a magnitude of completeness of 0.8.

4 Results

4.1 Seismicity Distribution

Earthquakes of the Quebrada system are unevenly distributed across the fault network with the majority of the seismicity occurring on Q4, Q3, and Q1 from west to east (Figure 2). Earthquakes on Q4 cluster into three distinct groups along the strike direction from -20 to 2 km at about 5 km depth, where the origin location coincides with the centroid of the earthquakes ($3.764^\circ\text{S}/103.615^\circ\text{W}$, Figure 2c and d). These earthquakes form a strike parallel strand that is south of the surface fault trace, indicating a non-vertical fault plane dipping at 68° towards the south. There is a diffuse seismicity cloud located in between -2 and 8 km along strike that is west of the ITSC S7. This cloud occupies the inner corner of the ridge-transform intersection (Q4-S7), but does not extend beyond eastern S7.

There are fewer earthquakes on Q3 compared to those on Q4. However, seismicity on Q3 aligns well with the bathymetric fabric, indicating a near-vertical fault plane (Figure 2e and f). Intriguingly, a band of ~ 1000 earthquakes extends ~ 25 km west be-

yond the actively slipping portion of Q3, presumably trending along an abandoned fault segment of Q3 (i.e. the fracture zone; Figure 2e). These observations challenge the conventional assumption that there is no relative motion along fracture zones in such RTF systems. In order to better visualize this configuration, we use a local coordinate system to plot seismicity with origin at $3.715^{\circ}\text{S}/103.520^{\circ}\text{W}$. A cluster of events spread a spatial footprint of ~ 3 km at -20 km along the strike direction and at 5 km depth (Figure 2e and f), which marks the edge of the detected earthquakes on the Q3 fault strand. We also observe some possible deep events along ITSC S8. We confirm the location of these earthquakes by performing a synthetic test as detailed below. Locations of these events are, however, relatively more uncertain than others in the catalog, because they are located 50 km from the two OBS arrays (Figure 1 and 2). Few earthquakes were identified along Q2, which could indicate a seismically quiescent fault strand, or, given the network configuration, could just be due our limited ability to resolve seismicity there.

Seismicity on Q1 shares resemblance with earthquakes on Q4. By projecting the earthquakes into a local coordinate with the origin at the centroid of the seismicity ($3.720^{\circ}\text{S}/102.972^{\circ}\text{W}$), we identify one group of earthquakes situated between 0 and 28 km that define a linear trend. This strand of earthquakes deviates away from the seafloor fault trace, suggesting a fault plane dipping $\sim 80^{\circ}$ towards the north (Figure 2g and h). Another diffuse group of earthquakes is located between -12 and 0 km along the strike direction. The diffuse pattern of these earthquakes is similar to those of Q4 reaching a deep depth up to 15 km towards the west. This cluster of earthquakes trends along an oblique direction east of ITSC S9 in the inner corner of the ridge-transform intersection (S9-Q1). There is an apparent group of earthquakes forming a strike-normal feature near ~ 30 km along the strike direction (shaded area in Figure 2h). However, this feature is not present in the catalog requiring events having at least 4 *P* and 4 *S* picks, suggesting its large uncertainties (Figure 2b and S5).

4.2 Spatiotemporal Earthquake Clusters

Seismicity seems to progress in space and time differently between the different Quebrada fault segments (Figure 3). To identify and analyze possible clusters of earthquakes, we first project the hypocenters into a 2D space-time domain with the space domain parallel to the mean fault strike direction (102°) and the time domain defined as Julian day of 2008. We then define earthquake clusters as those falling within a neighborhood-search radius of 1.3 and a minimum number of neighbors of 40 events using a density based clustering algorithm (e.g., function, `dbSCAN` MATLAB, 2018). Events not meeting this criterion for clustering are assumed to be isolated events (Ester et al., 1996). In order to test the sensitivity of our clustering approach to these parameters, we varied different parameter combinations, as given in Table S3. In general, larger neighborhood-searching radius and smaller minimum number of neighbors results in a greater number of (smaller) clusters. The preferred parameters here are determined by a trial and error approach, which balances the number and density of the clusters (Figure 3). This exercise recognizes several clusters on Q1, Q3, and Q4, and they are color coded by their occurrence time in Figure 3. The spatial centroids of each cluster are shown in Figure 4.

Along Q4, all the identified clusters are located within the seismicity cloud near the ridge-transform intersection. The seismicity cloud can be roughly divided into two subareas: a western part with some vertical-trending seismicity and an eastern part with more diffuse seismicity (Figure 4 and S7). The western portion is connected to the Q4 transform fault by a band of linear seismicity at ~ 5 km depth (Figure 4a). Events in this western sub-area are distributed from the seafloor to depths of 5 km, while seismicity extends deeper from ~ 5 km to 8 km as for the eastern subarea. In total, 12 clusters are identified within the Q4 seismicity cloud. Seven clusters were located in the western end of Q4, and five clusters were located in the eastern portion of Q4 (Figure S8). Cluster

317 1 is the largest cluster and is related to the increase in seismicity rate for about 20 days
 318 at the beginning of 2008 (Figure 4(d)). .

319 Seismicity abruptly progressed along Q4 around Julian day 6 (Figure 3d). This change
 320 might have been triggered by two $M \geq 3$ events on January 6 2008 (Table S2, Event 1 and
 321 2). We located these two events with a grid-search method using manually picked P -wave
 322 arrivals (Text S2), and their locations are within the Q4 cloud as shown in Figure S9.
 323 Events 1 and 2 are both located in the western part of the Q4 seismicity cloud, with event
 324 1 located at ~ 8 km depth to the east and event 2 to the west with its depth unresolved
 325 (Table S2). The event 1–2 sequence shows a clear migration pattern from east to west
 326 at a speed of ~ 0.8 km/hr (Figure S10).

327 Two clusters are identified on the Q3 fracture zone around day 135 (Figure 3b).
 328 The two clusters locate at about -20 km along the strike direction and at a depth of about
 329 5 km (Figure 2e and f). They correspond to the highest seismicity rate along Q3 dur-
 330 ing the experiment (Figure 3 (d)).

331 For Q1, we identified 17 temporal clusters in the diffuse cloud (Figure 4 and S11).
 332 The Q1 cloud has an apparent westward dipping feature towards the ITSC S9. However,
 333 there are no clear linear trending features in these clusters. The 17 clusters span across
 334 the whole diffuse cloud. Three clusters occurred on day 199, 202 and 203 are likely mi-
 335 grating sequences of events propagating from west to east, connecting the diffuse cloud
 336 to the transform fault Q1.

337 5 Discussion

338 5.1 Location Uncertainty

339 We evaluate the robustness of our hypocenter location estimates by performing syn-
 340 thetic resolvability experiments in the Q1 and Q4 diffuse clouds, and on the apparently
 341 abandoned fault segment of Q3. We use our final relocation results as input to gener-
 342 ate synthetic P and S arrival times using the same 1D velocity model used in the loca-
 343 tion procedure. For a given case, the synthetic arrival times are only computed for sta-
 344 tions that were used to locate the observed event. We further explore uncertainty by adding
 345 random, normally-distributed errors to the synthetic arrival times. We assume the dis-
 346 tributions have zero means but have independent standard deviations (σ) for P and S
 347 arrival times. We test three pairs of σ for the P and S arrival times as listed in Table S4.
 348 These values represent realistic picking errors as they are adopted from the training dataset
 349 of the EQTransformer algorithm (Mousavi et al., 2020). In total, we construct four sets
 350 of synthetic datasets, including one without random errors, and apply the COMPLOC
 351 algorithm to these arrival times to invert for earthquake locations (Lin & Shearer, 2005,
 352 2006).

353 We find the major tectonic trends defined by the hypocenters can be fully recov-
 354 ered for all four trial datasets. Epicentral location differences (i.e., latitude and longi-
 355 tude) between the synthetic and observed locations are generally less than 0.04° ($>99\%$,
 356 Figure S12–S13). Location differences for Q3 earthquakes that are on the active frac-
 357 ture zone segment are less than 0.01° ($>99\%$, Figure S13b). Hypocenter depth can be
 358 reliably resolved since the majority of earthquakes in the deep diffuse clouds are consis-
 359 tently located at depths of 5 to 10 km (Figure S14). Three-dimensional velocity varia-
 360 tions can also cause location biases, but are unlikely to distort the observed features be-
 361 cause of the relatively homogeneous velocity structures of the region (Roland et al., 2012).
 362 Clock drift of the OBSs could be another source of location errors (Gouédard et al., 2014),
 363 but such an effect is corrected by the instrument center and we do not observe clear dif-
 364 ferences in earthquake locations during the experiment period.

We note that the synthetic tests do not explore the true location uncertainties but only show that the key features can be recovered by the network configuration, and hence our tests likely represent a best case scenario. Therefore, we examine events with more than four P arrival picks and more than four S arrival picks, and only interpret features that are robustly resolved for this superior quality catalog (Figure S5). The major features discussed in Section 4 are also observed in this catalog (Figure S5), showing similar key features as for the whole catalog. In particular, seismicity on the Q3 fracture zone and in the two deep diffuse clouds are also located at similar locations as those in the full catalog (Figure S5). To further evaluate the diffuse cloud features at Q1 and Q4, we examine the cross correlation results from our relocation procedure and also further pairwise cross correlate all the events in the same cloud. The cross correlation results suggest limited similarities of the P or S waveforms (low cross correlation coefficients), indicating these earthquakes were unlikely from the same positions with the same focal mechanisms. Based on these tests, the reported features in the study are likely real.

5.2 Seismicity and Slip along Transform Faults

Except for the earthquakes in the two deep diffuse clouds, most of the microearthquakes that occurred on Q4, Q3 and Q1 are at a depth around 5 km, defining linear features oriented parallel to surface fault traces (Figure 2). The lack of earthquakes for fault patches shallower than 5 km depth seems to suggest that these fault patches are partially locked and greater earthquakes may occur there occasionally. However, the network configuration may have limited location resolution for shallower earthquakes, leaving the physical nature of the shallow fault patches uncertain. At Quebrada, the sharp contrast between the fast spreading rate (~ 123 mm/yr) and a lack of moderate magnitude earthquakes (only 73 $M > 3$ events since 1980) suggests that most of the plate spreading may have been accommodated by aseismic slip along these Quebrada faults. RTF segments that are dominated by aseismic slip, however, tend to have active microearthquakes that can extend into the uppermost mantle (McGuire et al., 2012). Such segments may have experienced higher degrees of damage compared to more intact patches that can host M6 earthquakes, such as the barrier zones of the Gofar and Discovery systems (McGuire et al., 2012; Wolfson-Schwehr et al., 2014). There are no such barrier zones observed in the Quebrada system. These apparent contrasts between Quebrada and other RTF systems are not consistent with current understanding of deformation partitioning at oceanic transform faults.

We observe few events on the Q2 fault, which could be due to the observational limit as our stations are away from the fault strand. Alternatively, the possible lack of seismicity could indicate that most of the displacement along Q2 is accommodated by aseismic slip, which may have resulted from the unusually thin crust (3–4 km) there in the deep basins (Pickle et al., 2009). This relatively thin crust could lead to a fault damage zone with a limited depth extent, and the deep basins might have been undergoing extension, which would cause a low normal stress on the Q2 segment. The combination of the two effects would favor aseismic slip, rather release of accumulated strain via large earthquakes (Liu & Rice, 2005; Liu et al., 2012). Such an interpretation can explain that a 17-year earthquake catalog on Quebrada detected much fewer events along Q2 than on other three segments, and there are no $M > 5.5$ events found on Q2 segment either (McGuire, 2008). We further speculate that the deformation mechanisms controlling Q2 and other Quebrada faults are likely different, given the varying seismicity and possibly distinct crustal structures.

Surprisingly, we observe abundant seismicity on the fracture zone segment of the Q3 transform fault, which contradicts the conventional idea that no relative slip occurs along fracture zones (Tucholke & Schouten, 1988; Engdahl et al., 1998; Bondár & Storchak, 2011). The presence of these earthquakes suggests relative motion on either side of the Q3 fracture zone, and the strike of Q3 (98°) is different from those of Q1 and Q4

(102°; Figure S15). These combined observations could be explained by a local rotation within the Quebrada system. This rotation is consistent with the suggested clockwise change in rotation of the plate spreading direction between the Pacific and Nazca plates over the past few million years (Lonsdale, 1989). The clockwise rotation in plate spreading direction is inferred from the trend of several multi-strand transform systems in the southern EPR (Lonsdale, 1989), and is hence tentative. Nonetheless, S9 is the youngest and shortest ITSC (4 km) among the Quebrada spreading centers (Pickle et al., 2009), meaning that accommodating this change in spreading direction may be easier there than on other ITSCs in the system. Hence the Q3 fault could be undergoing clockwise rotation in order to reach equilibrium with the current spreading direction, which could explain the observed seismicity on the Q3 fracture zone.

428 5.3 Diffuse Seismicity

429 One of the most striking features of the Quebrada catalog presented here is the pair
 430 of diffuse clouds of seismicity at the inside corners of the ridge-transform intersections
 431 at Q1-S9 and Q4-R7. These earthquakes form two dipping trends, which deepen towards
 432 the ITSCs, with earthquakes mostly located at depths of 5 to 10 km. These earthquakes
 433 are considerably deeper than other events in the region (Figure 4). A regional three-dimensional
 434 thermal model shows that the Quebrada area is relatively cooler than the neighboring
 435 Discovery-Gofar system, and predicts that the depth of 1000°C isotherm is 8–10 km at
 436 Quebrada (Pickle et al., 2009). Since earthquakes in the two diffuse zones are observed
 437 within this depth window, which is beyond the typical frictional stability transition at
 438 ~500–600°C (Boettcher et al., 2007; He et al., 2007), additional mechanisms, not included
 439 in the thermal model, are likely required to explain the deep seismicity.

440 Two diffuse clouds co-locate within the deep basins, and we infer that the same ex-
 441 tensional processes that have formed the basins may also explain the origin of these earth-
 442 quakes. In conjunction with the possibility of small-scale rotation, transtension could
 443 create damage zones at the inside corners of the ridge-transform intersections. Because
 444 of the continuous rotation, these damage zones could lead to enhanced permeability, and
 445 promote enhanced fluid circulation through the crust and upper mantle, and thus lower
 446 ambient temperatures (Schlindwein & Schmid, 2016; Grevemeyer et al., 2019; Schlindwein,
 447 2020). Such processes may favor the generation of serpentine, talc, or other altered min-
 448 eral phases in the upper mantle, leading to heterogeneous stress conditions and distributed
 449 seismicity. This distributed pattern of alteration and deformation could explain the ob-
 450 served clusters in the two deep clouds, the apparent lack of systematic migration pat-
 451 terns in the clouds, and bursts of seismicity which could be driven by localized episodes
 452 of fluid circulation (Figure 4, S8, and S11).

453 Alternatively, the presence of high-temperature fractures under high temperature
 454 conditions in the semiductile mylonites (Yu et al., 2021) or coarse-grained peridotite can
 455 also sustain brittle behaviour at greater pressure-temperature conditions (Kohli et al.,
 456 2021). Such processes could have facilitated the observed deep seismicity at 8–10 km depth
 457 without significant reduction in the mantle temperatures. For example, deep fluid-rock
 458 interaction, weakening and strain localization within the oceanic lithosphere beneath trans-
 459 form faults can cause brittle fracture at temperatures over 800°C (Prigent et al., 2020).
 460 In all possible scenarios, fluids likely have played an important role in generating the deep,
 461 diffuse seismicity. The small-scale rotation and extension at the transform fault and ITSC
 462 intersections might have created fluid circulation pathways and further facilitated the
 463 interaction between fluid and oceanic lithosphere.

464 The deepening trend of the two seismicity clouds towards ITSCs might relate to
 465 melt migration and/or faulting induced enhanced hydrothermal circulation. Models of
 466 three-dimensional melt flow at segmented transform systems show that melt associated
 467 with relatively short ITSCs is likely to migrate towards adjacent, longer spreading seg-

468 ments (Gregg et al., 2009). In this model, depth to the top of the melt is deeper at the
469 ITSC and shallower at the adjacent mid-ocean ridge, sharing a similar geometry as the
470 dipping structure of the seismicity clouds observed at Quebrada. If a comparable melt
471 flow regime applies to the Quebrada system, the intense seismicity clouds might reflect
472 an ongoing extraction of melt at the ITSCs towards the adjacent spreading segments.
473 However, the causality between the melt migration and intense seismicity at the ridge-
474 transform intersection is unclear. For example, the melt migration and seismicity dis-
475 tribution might both be by-products of other physical mechanisms, such as the three-
476 dimensional thermal and stress redistribution due to the ridge-transform intersection.
477 Faulting process due to temporally discontinuous or spatially heterogeneous rotation could
478 be another explanation for the observed seismicity. Although the earthquake clouds have
479 a diffuse rather than planer geometry, they might represent an earlier stage of the open-
480 ing of the pull-apart basin, due to the rotation of the Quebrada fault system in response
481 to the current plate spreading direction. Furthermore, the Q4 diffuse cloud is moderately
482 more focused than that of Q1, which is consistent with the inference that S9 is the most
483 recently developed ITSC in the Quebrada transform system (Pickle et al., 2009). The
484 two diffuse clouds are located in the inside corners of the spreading center and transform
485 fault intersections, which indicates possible differences between the two sides of the ITSCs
486 in terms of stress state, fluid circulation, melt supply, and material properties.

487 6 Conclusions

488 We use seven months of OBS data to detect and locate 23,593 earthquakes on mul-
489 tiple strands of the Quebrada transform fault system. Three of the four transform faults
490 (Q1, Q3, and Q4) are seismically active, while the other fault segment (Q2) likely slips
491 aseismically. We find abundant seismicity along the (supposedly inactive) Q3 fracture
492 zone, and a pair of diffuse seismicity clouds associated with transform faults Q1 and Q4.
493 These two clouds are at the inside corners of the intersections between the ITSCs and
494 the transform faults, extend into the uppermost mantle (5–10 km), and deepen towards
495 the ITSCs. We infer that brittle deformation associated with these deep clouds is related
496 to enhanced fluid circulation down to upper mantle that might have lowered the man-
497 tle temperature or weakened the oceanic lithosphere through fluid-rock interactions. Such
498 effects may relate to heterogeneous rotational motions within the Quebrada system, which
499 could explain the active abandoned fault of Q3. We speculate that the tectonic processes
500 and displacement on these multi-strand transform faults likely experience positive feed-
501 backs, and that atypical earthquakes are caused by local small-scale rotations in response
502 to regional changes in plate spreading direction.

Open Research

The seismic data are available from the Data Management Center (DMC) of the Incorporated Research Institutions for Seismology (IRIS) under the network codes ZD. IRIS Data Services, and the IRIS Data Management Center, were used to access waveforms, related metadata, and derived products used in this study. IRIS Data Services are funded through the Seismological Facilities for the Advancement of Geoscience and EarthScope (SAGE) Proposal of the National Science Foundation (NSF) under Cooperative Agreement EAR-1261681. The earthquake catalog was downloaded from the International Seismological Center (ISC) and the bathymetry data can be obtained from <https://www.ngdc.noaa.gov/maps/autogrid/>. We used open-source software EQTransformer (Mousavi et al., 2020), REAL (M. Zhang et al., 2019), COMPLOC (Lin & Shearer, 2006) and GrowClust (Trugman & Shearer, 2017) for earthquake detection, association, location and re-location. The earthquake catalog is included in the supplementary material and is also archived at Marine Geoscience Data System, Cruise DOI: 10.26022/IEDA/330427 (<http://get.iedadata.org/doi/330427>).

Acknowledgments

We thank the editor Dr. Lucy Flesch and Dr. Monica Wolfson-Schwehr for their thoughtful and constructive reviews of the paper. J.G and W.F acknowledge support from National Science Foundation (NSF) grant OCE-1833279. The ocean bottom seismometer instruments were provided by the Ocean Bottom Seismograph Instrument Center (OB-SIP). The authors thank Jeffrey McGuire, John Collins, and the rest of the 2008 Quebrada-Discovery-Gofar experiment team for collecting and archiving the data. The authors thank Peter Shearer for teaching us the COMPLOC and GrowClust software.

Accepted Article

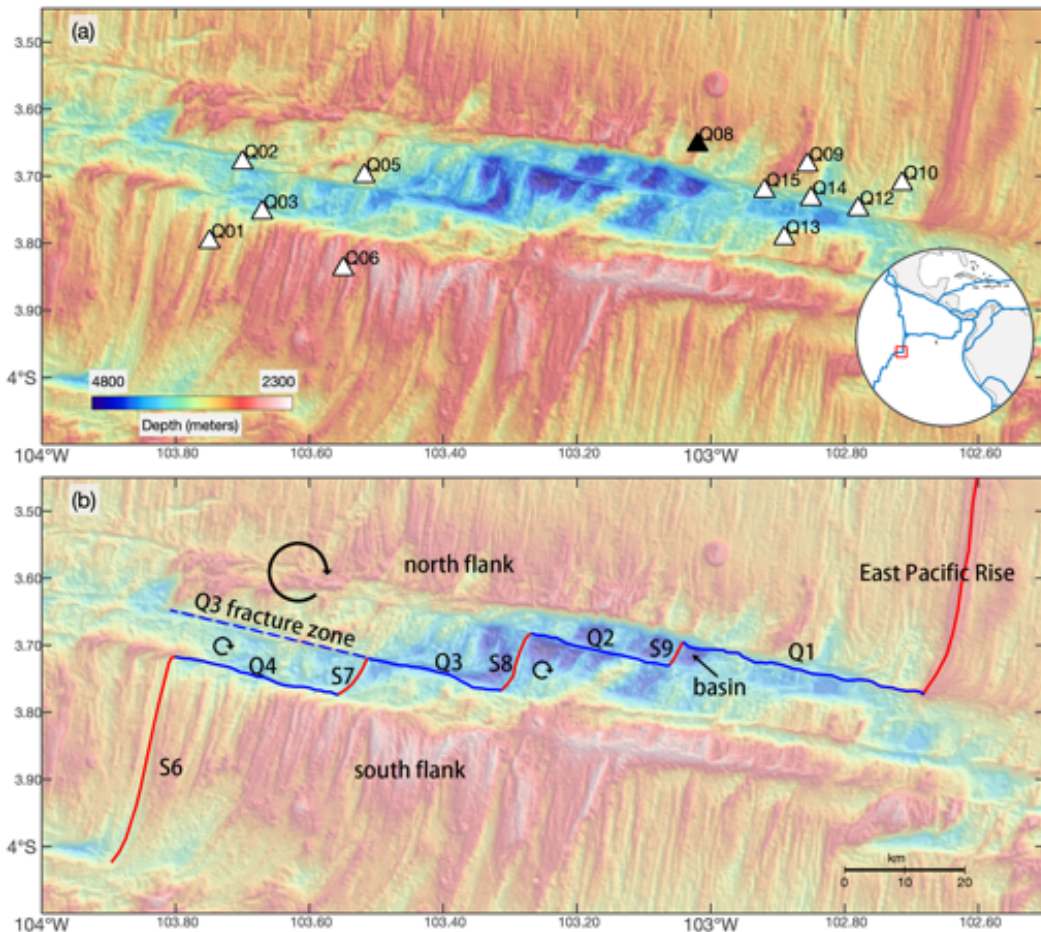


Figure 1. Bathymetry and structural interpretation of study area. (a) Bathymetry of study area. White labelled triangles are the 11 OBS stations that worked normally during the experiment. Station Q08 malfunctioned during the experiment. Inset shows location of study area at East Pacific Rise. (b) Structural interpretation of study area. Q1, Q2, Q3 and Q4 are surface traces of four segments of Quebrada transform system; S6, S7, S8 and S9 are ITSCs, following naming convention of Pickle et al. (2009); dashed line to the west of Q3 denotes Q3 fracture zone; basins and bathymetric highs (flanks) are also denoted on the maps. Circle arrows show the interpreted clock-wise rotation of the system.

Accepted Article

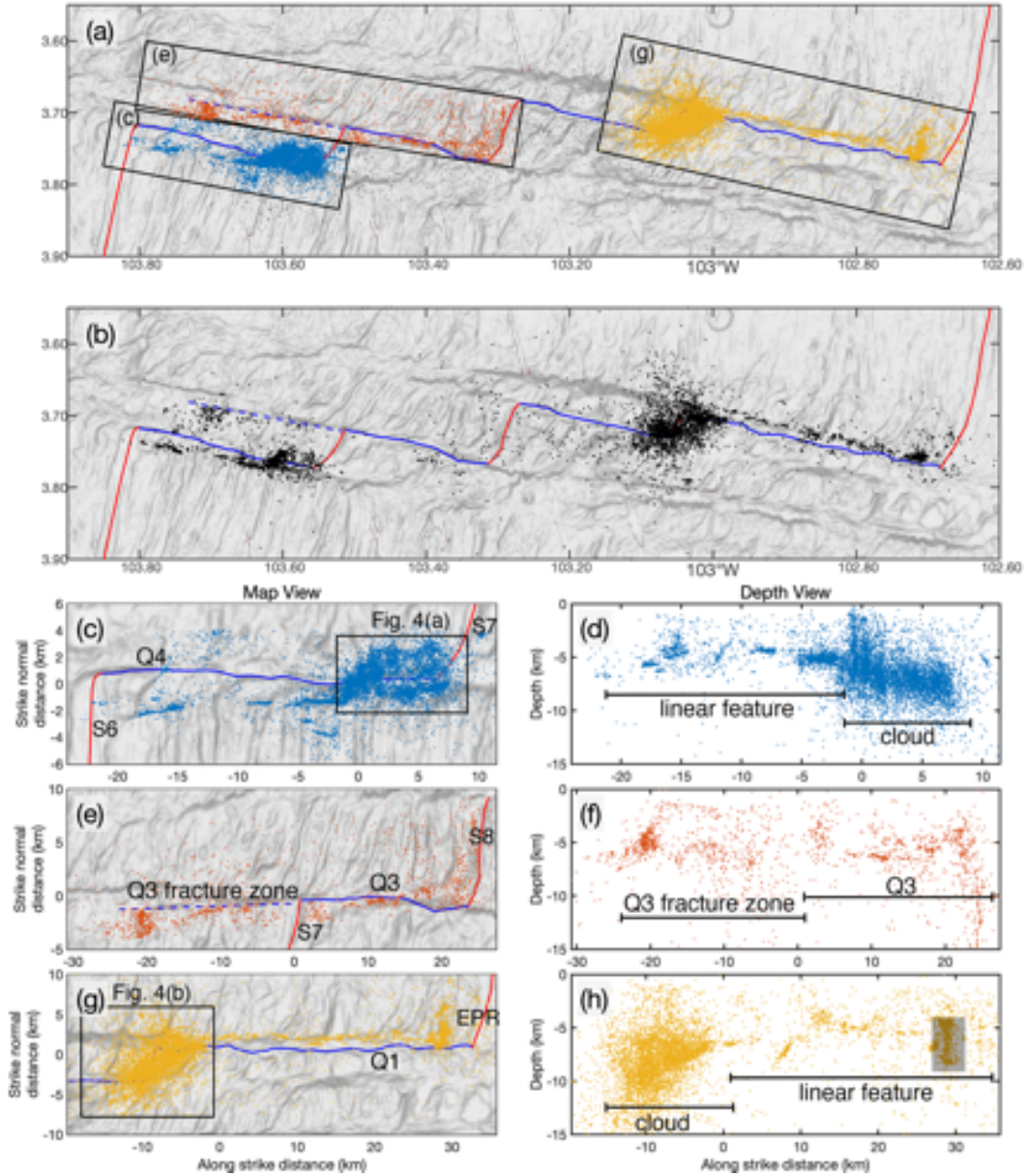


Figure 2. Earthquake hypocenters. (a) Map view of earthquake locations from the full catalog, with shaded relief background. Three rectangular boxes denote the subset of events on Q4, Q3 and Q1, respectively. Blue, red and blue dashed lines are surface traces of transform faults, ITSCs and Q3 fracture zone, respectively. (b) Map view of earthquake locations for events with more than 4 P - and 4 S -picks. (c) to (h) Zoom-in map and depth profiles of seismicity on faults Q4, Q3 and Q1. Blue lines denote transform fault surface traces. Blue dashed line denotes Q3 fracture zone. Red lines denote ITSCs and EPR. The two boxes in (c) and (g) highlight the two clouds of seismicity at the inside corners of the ridge-transform intersections (Figure 4). Gray shaded region in (h) indicates where earthquake locations are more uncertain.

Accepted Article

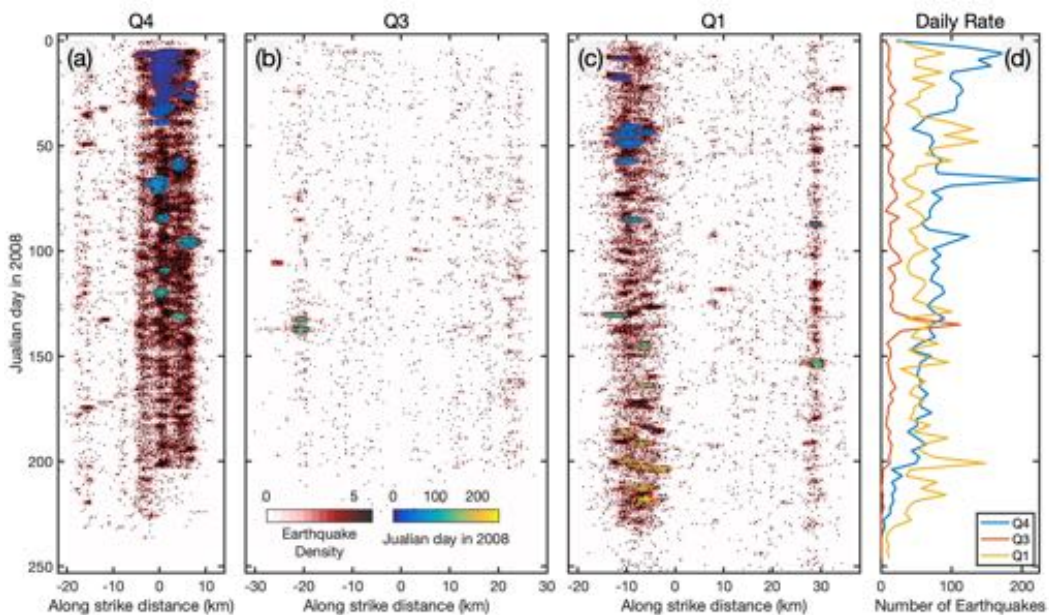


Figure 3. Spatiotemporal evolution of the Quebrada microearthquakes. (a) to (c) Spatiotemporal evolution of seismicity on Q4, Q3 and Q1 in the three rectangular boxes in Figure 2, respectively. Black dots are earthquakes plotted on top of a red scale earthquake density plot. Colored zones are clusters identified along each fault segment. (d) Daily seismicity rates of Q4, Q3 and Q1 that are summed over every 2 days.

Accepted Article

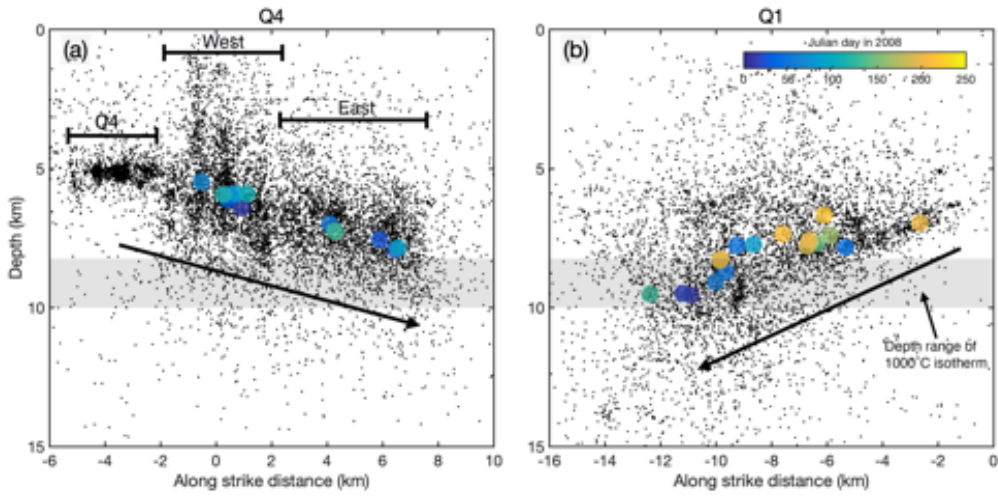


Figure 4. Depth profiles through two seismicity clouds in Figure 2 and the centroid locations of clusters in Figure 3. (a) Q4 seismicity cloud and (b) Q1 seismicity cloud. Black dots show earthquakes. Filled colored circles denote the centroids of seismicity clusters. Black bars in (a) indicate the seismicity that are associated with Q4 transform faults, and the west and the east parts of the Q4 seismicity cloud. Black arrows in (a) and (b) denote the inferred dipping directions of the seismicity clouds. The transparent gray bands show a depth range (8 to 10 km) of 1000°C isotherm for the ambient mantle at the Quebrada system from Pickle et al. (2009).

526 **References**

- 527 Bird, P. (2003). An updated digital model of plate boundaries. *Geochemistry, Geo-*
528 physics, Geosystems, 4(3). doi: <https://doi.org/10.1029/2001GC000252>
- 529 Boettcher, M. S., Hirth, G., & Evans, B. (2007). Olivine friction at the base of
oceanic seismogenic zones. *Journal of Geophysical Research: Solid Earth*,
112(B1).
- 530 Boettcher, M. S., & Jordan, T. H. (2004). Earthquake scaling relations for mid-
ocean ridge transform faults. *Journal of Geophysical Research: Solid Earth*,
109(B12). doi: <https://doi.org/10.1029/2004JB003110>
- 531 Boettcher, M. S., & McGuire, J. J. (2009). Scaling relations for seismic cycles on
mid-ocean ridge transform faults. *Geophysical Research Letters*, 36(21). doi:
<https://doi.org/10.1029/2009GL040115>
- 532 Bondár, I., & Storchak, D. (2011). Improved location procedures at the interna-
tional seismological centre. *Geophysical Journal International*, 186(3), 1220-
1244. doi: <https://doi.org/10.1111/j.1365-246X.2011.05107.x>
- 533 Contreras-Reyes, E., & Carrizo, D. (2011). Control of high oceanic features and
subduction channel on earthquake ruptures along the ChilePeru subduction
zone. *Physics of the Earth and Planetary Interiors*, 186(1), 49-58. doi:
<https://doi.org/10.1016/j.pepi.2011.03.002>
- 534 Engdahl, E. R., van der Hilst, R., & Buland, R. (1998). Global teleseismic earth-
quake relocation with improved travel times and procedures for depth determi-
nation. *Bulletin of the Seismological Society of America*, 88(3), 722-743. doi:
10.1785/BSSA0880030722
- 535 Ester, M., Kriegel, H., Sander, J., & Xu, X. (1996, August). A density-based
algorithm for discovering clusters in large spatial databases with noise. In
*Proceedings of the second international conference on knowledge discovery in
databases and data mining* (p. 226-231). AAAI Press.
- 536 Fox, C. G., Matsumoto, H., & Lau, T.-K. A. (2001). Monitoring pacific ocean
seismicity from an autonomous hydrophone array. *Journal of Geophysical
Research: Solid Earth*, 106(B3), 4183-4206. doi: <https://doi.org/10.1029/2000JB900404>
- 537 Fox, P. J., & Gallo, D. G. (1984). A tectonic model for ridge-transform-ridge plate
boundaries: Implications for the structure of oceanic lithosphere. *Tectono-
physics*, 104(3), 205-242. doi: [https://doi.org/10.1016/0040-1951\(84\)90124-0](https://doi.org/10.1016/0040-1951(84)90124-0)
- 538 Gouédard, P., Seher, T., McGuire, J. J., Collins, J. A., & van der Hilst, R. D.
(2014). Correction of ocean-bottom seismometer instrumental clock errors
using ambient seismic noise. *Bulletin of the Seismological Society of America*,
104(3), 1276-1288.
- 539 Gregg, P. M., Behn, M. D., Lin, J., & Grove, T. L. (2009). Melt generation, crystal-
lization, and extraction beneath segmented oceanic transform faults. *Journal
of Geophysical Research: Solid Earth*, 114(B11). doi: <https://doi.org/10.1029/2008JB006100>
- 540 Grevemeyer, I., Hayman, N. W., Lange, D., Peirce, C., Papenberg, C., Van Aven-
donk, H. J., ... Dannowski, A. (2019). Constraining the maximum depth of
brittle deformation at slow- and ultraslow-spreading ridges using microseismic-
ity. *Geology*, 47(11), 1069-1073. doi: 10.1130/G46577.1
- 541 Guo, H., Zhang, H., & Froment, B. (2018). Structural control on earthquake be-
haviors revealed by high-resolution Vp/Vs imaging along the Gofar transform
fault, East Pacific Rise. *Earth and Planetary Science Letters*, 499, 243-255.
doi: <https://doi.org/10.1016/j.epsl.2018.07.037>
- 542 Gutenberg, B., & Richter, C. F. (1956, 04). Earthquake magnitude, intensity, en-
ergy, and acceleration: (Second paper). *Bulletin of the Seismological Society of
America*, 46(2), 105-145. doi: 10.1785/BSSA0460020105
- 543 Hall, C. E., Gurnis, M., Sdrolias, M., Lavier, L. L., & Mller, R. (2003). Cata-
strophic initiation of subduction following forced convergence across frac-

- ture zones. *Earth and Planetary Science Letters*, 212(1), 15-30. doi: [https://doi.org/10.1016/S0012-821X\(03\)00242-5](https://doi.org/10.1016/S0012-821X(03)00242-5)
- Hauksson, E., & Shearer, P. (2005). Southern California hypocenter relocation with waveform cross-correlation, Part 1: Results using the double-difference method. *Bulletin of the Seismological Society of America*, 95(3), 896-903. doi: 10.1785/0120040167
- He, C., Wang, Z., & Yao, W. (2007). Frictional sliding of gabbro gouge under hydrothermal conditions. *Tectonophysics*, 445(3-4), 353–362.
- International Seismological Centre. (2021). On-line bulletin. doi: <https://doi.org/10.31905/D808B830>
- Kohli, A., Wolfson-Schwehr, M., Prigent, C., & Warren, J. M. (2021, Aug 01). Oceanic transform fault seismicity and slip mode influenced by seawater infiltration. *Nature Geoscience*, 14(8), 606-611. doi: 10.1038/s41561-021-00778-1
- Kuna, V. M., Nábělek, J. L., & Braumiller, J. (2019, Feb 01). Mode of slip and crust–mantle interaction at oceanic transform faults. *Nature Geoscience*, 12(2), 138-142. doi: 10.1038/s41561-018-0287-1
- Lange, D., Tilmann, F., Rietbrock, A., Collings, R., Natawidjaja, D. H., Suwargadi, B. W., ... Ryberg, T. (2010). The fine structure of the subducted Investigator Fracture Zone in western Sumatra as seen by local seismicity. *Earth and Planetary Science Letters*, 298(1), 47-56. doi: <https://doi.org/10.1016/j.epsl.2010.07.020>
- Lin, G., & Shearer, P. (2005). Tests of relative earthquake location techniques using synthetic data. *Journal of Geophysical Research: Solid Earth*, 110(B4). doi: <https://doi.org/10.1029/2004JB003380>
- Lin, G., & Shearer, P. (2006). The COMPLLOC earthquake location package. *Seismological Research Letters*, 77(4), 440-444.
- Liu, Y., McGuire, J. J., & Behn, M. D. (2012). Frictional behavior of oceanic transform faults and its influence on earthquake characteristics. *Journal of Geophysical Research: Solid Earth*, 117(B4). doi: <https://doi.org/10.1029/2011JB009025>
- Liu, Y., & Rice, J. R. (2005). Aseismic slip transients emerge spontaneously in three-dimensional rate and state modeling of subduction earthquake sequences. *Journal of Geophysical Research: Solid Earth*, 110(B8). doi: <https://doi.org/10.1029/2004JB003424>
- Lonsdale, P. (1989). Segmentation of the Pacific-Nazca Spreading Center, 1°N20°S. *Journal of Geophysical Research: Solid Earth*, 94(B9), 12197-12225. doi: <https://doi.org/10.1029/JB094iB09p12197>
- Macdonald, K. C. (1982). Mid-ocean ridges: Fine scale tectonic, volcanic and hydrothermal processes within the plate boundary zone. *Annual Review of Earth and Planetary Sciences*, 10(1), 155-190. doi: 10.1146/annurev.ea.10.050182.001103
- MATLAB. (2018). 9.7.0.1190202 (r2019b). Natick, Massachusetts: The MathWorks Inc.
- McGuire, J. J. (2008). Seismic cycles and earthquake predictability on East Pacific Rise transform faults. *Bulletin of the Seismological Society of America*, 98(3), 1067-1084. doi: 10.1785/0120070154
- McGuire, J. J., Collins, J. A., Gouédard, P., Roland, E., Lizarralde, D., Boettcher, M. S., ... van der Hilst, R. D. (2012). Variations in earthquake rupture properties along the Gofar transform fault, East Pacific Rise. *Nature Geoscience*, 5(5), 336-341. doi: 10.1038/ngeo1454
- Menard, H. W., & Atwater, T. (1968). Changes in direction of sea floor spreading. *Nature*, 219(5153), 463-467. doi: 10.1038/219463a0
- Morgan, J. P., & Forsyth, D. W. (1988). Three-dimensional flow and temperature perturbations due to a transform offset: Effects on oceanic crustal and upper mantle structure. *Journal of Geophysical Research: Solid Earth*, 93(B4),

- 2955-2966. doi: <https://doi.org/10.1029/JB093iB04p02955>
- Mousavi, S. M., Ellsworth, W. L., Zhu, W., Chuang, L. Y., & Beroza, G. C. (2020). Earthquake transformer—an attentive deep-learning model for simultaneous earthquake detection and phase picking. *Nature Communications*(1), 3952. doi: 10.1038/s41467-020-17591-w
- Mousavi, S. M., Sheng, Y., Zhu, W., & Beroza, G. C. (2019). STanford EArthquake Dataset (STEAD): A global data set of seismic signals for AI. *IEEE Access*, 7, 179464-179476. doi: 10.1109/ACCESS.2019.2947848
- Parmentier, E. M., & Forsyth, D. W. (1985). Three-dimensional flow beneath a slow spreading ridge axis: A dynamic contribution to the deepening of the median valley toward fracture zones. *Journal of Geophysical Research: Solid Earth*, 90(B1), 678-684. doi: <https://doi.org/10.1029/JB090iB01p00678>
- Parnell-Turner, R., Sohn, R., Peirce, C., Reston, T., MacLeod, C., Searle, R., & Simão, N. (2017). Oceanic detachment faults generate compression in extension. *Geology*, 45(10), 923–926.
- Pickle, R. C., Forsyth, D. W., Harmon, N., Nagle, A. N., & Saal, A. (2009). Thermo-mechanical control of axial topography of intra-transform spreading centers. *Earth and Planetary Science Letters*, 284(3), 343-351. doi: <https://doi.org/10.1016/j.epsl.2009.05.004>
- Pockalny, R. A. (1997). Evidence of transpression along the Clipperton Transform: Implications for processes of plate boundary reorganization. *Earth and Planetary Science Letters*, 146(3), 449-464. doi: [https://doi.org/10.1016/S0012-821X\(96\)00253-1](https://doi.org/10.1016/S0012-821X(96)00253-1)
- Pockalny, R. A., Fox, P. J., Fornari, D. J., Macdonald, K. C., & Perfit, M. R. (1997). Tectonic reconstruction of the Clipperton and Siqueiros Fracture Zones: Evidence and consequences of plate motion change for the last 3 Myr. *Journal of Geophysical Research: Solid Earth*, 102(B2), 3167-3181. doi: <https://doi.org/10.1029/96JB03391>
- Prigent, C., Warren, J., Kohli, A., & Teyssier, C. (2020). Fracture-mediated deep seawater flow and mantle hydration on oceanic transform faults. *Earth and Planetary Science Letters*, 532, 115988. doi: <https://doi.org/10.1016/j.epsl.2019.115988>
- Richards-Dinger, K. B., & Shearer, P. M. (2000). Earthquake locations in southern California obtained using source-specific station terms. *Journal of Geophysical Research: Solid Earth*, 105(B5), 10939-10960. doi: <https://doi.org/10.1029/2000JB900014>
- Robinson, D. P. (2011). A rare great earthquake on an oceanic fossil fracture zone. *Geophysical Journal International*, 186(3), 1121-1134. doi: 10.1111/j.1365-246X.2011.05092.x
- Roland, E., Lizarralde, D., McGuire, J. J., & Collins, J. A. (2012). Seismic velocity constraints on the material properties that control earthquake behavior at the Quebrada-Discovery-Gofar transform faults, East Pacific Rise. *Journal of Geophysical Research: Solid Earth*, 117(B11). doi: <https://doi.org/10.1029/2012JB009422>
- Ross, Z. E., Trugman, D. T., Hauksson, E., & Shearer, P. M. (2019). Searching for hidden earthquakes in Southern California. *Science*, 364(6442), 767-771. doi: 10.1126/science.aaw6888
- Schlindwein, V. (2020, 05). Constraining the maximum depth of brittle deformation at slow- and ultraslow-spreading ridges using microseismicity: COMMENT. *Geology*, 48(5), e501-e501. doi: 10.1130/G47444C.1
- Schlindwein, V., & Schmid, F. (2016, Jul 01). Mid-ocean-ridge seismicity reveals extreme types of ocean lithosphere. *Nature*, 535(7611), 276-279. doi: 10.1038/nature18277
- Searle, R. C. (1983). Multiple, closely spaced transform faults in fast-slipping fracture zones. *Geology*, 11(10), 607-610.

- 691 Shi, P., Wei, M. M., & Pockalny, R. A. (2021). The ubiquitous creeping segments on
 692 oceanic transform faults. *Geology*. doi: 10.1130/G49562.1
- 693 Smith, W. H. F., & Sandwell, D. T. (1997). Global sea floor topography from satel-
 694 lite altimetry and ship depth soundings. *Science*, 277(5334), 1956-1962. doi:
 695 10.1126/science.277.5334.1956
- 696 Tan, Y. J., Tolstoy, M., Waldhauser, F., & Wilcock, W. S. D. (2016, Dec 01).
 697 Dynamics of a seafloor-spreading episode at the East Pacific Rise. *Nature*,
 698 540(7632), 261-265. doi: 10.1038/nature20116
- 699 Trugman, D. T., & Shearer, P. M. (2017). GrowClust: A hierarchical clustering
 700 algorithm for relative earthquake relocation, with application to the Spanish
 701 Springs and Sheldon, Nevada, earthquake sequences. *Seismological Research
 702 Letters*, 88(2A), 379-391.
- 703 Tucholke, B., & Schouten, H. (1988). Kane fracture zone. *Marine Geophysical Re-
 704 searches*, 10(1-2), 1-39.
- 705 Van Avendonk, H. J. A., Harding, A. J., Orcutt, J. A., & McClain, J. S. (1998). A
 706 two-dimensional tomographic study of the Clipperton transform fault. *Journal
 707 of Geophysical Research: Solid Earth*, 103(B8), 17885-17899. doi: <https://doi.org/10.1029/98JB00904>
- 708 Van Avendonk, H. J. A., Harding, A. J., Orcutt, J. A., & McClain, J. S. (2001).
 709 Contrast in crustal structure across the Clipperton transform fault from travel
 710 time tomography. *Journal of Geophysical Research: Solid Earth*, 106(B6),
 711 10961-10981. doi: <https://doi.org/10.1029/2000JB900459>
- 712 Waldhauser, F., & Ellsworth, W. L. (2000). A Double-Difference Earthquake Lo-
 713 cation Algorithm: Method and Application to the Northern Hayward Fault,
 714 California. *Bulletin of the Seismological Society of America*, 90(6), 1353-1368.
 715 doi: 10.1785/0120000006
- 716 Wang, R., Schmandt, B., Zhang, M., Glasgow, M., Kiser, E., Rysanek, S., &
 717 Stairs, R. (2020). Injection-induced earthquakes on complex fault zones
 718 of the Raton basin illuminated by machine-learning phase picker and dense
 719 nodal array. *Geophysical Research Letters*, 47(14), e2020GL088168. doi:
 720 <https://doi.org/10.1029/2020GL088168>
- 721 Wolfson-Schwehr, M., & Boettcher, M. S. (2019). Global characteristics of oceanic
 722 transform fault structure and seismicity. In J. C. Duarte (Ed.), *Transform
 723 plate boundaries and fracture zones* (p. 2159). Amsterdam: Elsevier.
- 724 Wolfson-Schwehr, M., Boettcher, M. S., & Behn, M. D. (2017). Thermal segmen-
 725 tation of mid-ocean ridge-transform faults. *Geochemistry, Geophysics, Geosys-
 726 tems*, 18(9), 3405-3418. doi: <https://doi.org/10.1002/2017GC006967>
- 727 Wolfson-Schwehr, M., Boettcher, M. S., McGuire, J. J., & Collins, J. A. (2014).
 728 The relationship between seismicity and fault structure on the Discovery trans-
 729 form fault, East Pacific Rise. *Geochemistry, Geophysics, Geosystems*, 15(9),
 730 3698-3712. doi: <https://doi.org/10.1002/2014GC005445>
- 731 Yu, Z., Singh, S. C., Gregory, E. P. M., Maia, M., Wang, Z., & Brunelli, D. (2021).
 732 Semibrittle seismic deformation in high-temperature mantle mylonite shear
 733 zone along the romanche transform fault. *Science Advances*, 7(15), eabf3388.
 734 doi: 10.1126/sciadv.abf3388
- 735 Zhang, H., & Thurber, C. H. (2003). Double-difference tomography: The method
 736 and its application to the Hayward fault, California. *Bulletin of the Seismolog-
 737 ical Society of America*, 93(5), 1875-1889. doi: 10.1785/0120020190
- 738 Zhang, M., Ellsworth, W. L., & Beroza, G. C. (2019). Rapid earthquake association
 739 and location. *Seismological Research Letters*, 90(6), 2276-2284.